

## THE FORMATION OF *IRIS* DIAGNOSTICS IX. THE FORMATION OF THE C I 135.58 NM LINE IN THE SOLAR ATMOSPHERE

HSIAO-HSUAN LIN<sup>1</sup>, MATS CARLSSON<sup>1</sup>, AND JORRIT LEENAARTS<sup>2,1</sup>

<sup>1</sup> Institute of Theoretical Astrophysics, University of Oslo, P.O. Box 1029 Blindern, NO-0315 Oslo, Norway and

<sup>2</sup> Institute for Solar Physics, Department of Astronomy, Stockholm University, AlbaNova University Centre, SE-106 91 Stockholm, Sweden  
*Draft version November 4, 2021*

### ABSTRACT

The C I 135.58 nm line is located in the wavelength range of NASA's *Interface Region Imaging Spectrograph* (*IRIS*) small explorer mission. We here study the formation and diagnostic potential of this line by means of non local-thermodynamic-equilibrium modeling, employing both 1D and 3D radiation-magnetohydrodynamic models. The C I/C II ionization balance is strongly influenced by photoionization by Ly $\alpha$  emission. The emission in the C I 135.58 nm line is dominated by a recombination cascade and the line forming region is optically thick. The Doppler shift of the line correlates strongly with the vertical velocity in its line forming region, which is typically located at 1.5 Mm height. With *IRIS* the C I 135.58 nm line is usually observed together with the O I 135.56 nm line, and from the Doppler shift of both lines, we obtain the velocity difference between the line forming regions of the two lines. From the ratio of the C I/O I line core intensity, we can determine the distance between the C I and the O I forming layers. Combined with the velocity difference, the velocity gradient at mid-chromospheric heights can be derived. The C I/O I total intensity line ratio is correlated with the inverse of the electron density in the mid-chromosphere. We conclude that the C I 135.58 nm line is an excellent probe of the middle chromosphere by itself, and together with the O I 135.56 nm line the two lines provide even more information, which complements other powerful chromospheric diagnostics of *IRIS* such as the Mg II h and k lines and the C II lines around 133.5 nm.

**Keywords:** Radiative transfer – Sun: atmosphere – Sun: chromosphere – Sun: UV radiation

### 1. INTRODUCTION

The C I 135.58 nm line ( $2s^2 2p^2 \ ^1D_2 - 2s^2 2p4d \ ^1F_3^o$ ) is in the wavelength range of the NASA small explorer mission *Interface Region Imaging Spectrograph* (*IRIS*) and is normally observed together with the nearby O I 135.56 nm line (Lin & Carlsson 2015). Their line cores are formed in the mid-chromosphere, unlike other strong lines that *IRIS* covers, such as Mg II h and k (Leenaarts et al. 2013a,b; Pereira et al. 2013) and the C II 133.5 nm multiplet (Rathore & Carlsson 2015; Rathore et al. 2015a,b), whose cores usually form in the upper chromosphere or transition region.

Already, the SKYLAB mission revealed interesting behavior of the C I/O I line ratio: during a solar flare, the C I 135.58 nm line gets stronger than the O I 135.56 nm line, the opposite of the behavior in the quiet Sun (Cheng et al. 1980). It is thus clear that the C I 135.58 nm line may provide diagnostics of the solar chromosphere, especially when combined with observations in the O I 135.56 nm line.

Lites & Cook (1979) modeled C I-C IV with semi-empirical models of flares. The C I 123.9 nm continuum is blended with the Ly $\alpha$  wing and the hydrogen radiative transfer was therefore solved together with carbon to take into account the effect of Ly $\alpha$  on the C I/C II ionization balance. It is important to include effects of partial redistribution (PRD) in the Ly $\alpha$  line profile. According to their calculations, the C I/C II ionization balance depends on the Ly $\alpha$  wing intensity and the Lyman continuum, but is insensitive to C I line transfer.

Mauas et al. (1989) presented a more complete study of the carbon line-formation problem, focussing on the C I 156.1 nm and 165.7 nm lines, based on the VAL3C semi-empirical model (Vernazza et al. 1981). The authors found that the

upper levels of these transitions are mostly populated by radiative recombination to highly excited levels, followed by radiative cascading. The central reversals in the calculated lines were deeper than in the observations. This could be due to only including four levels with higher excitation potential than the upper levels of the studied transitions, thus underestimating the radiative recombination, or it could be due to an underestimate of the radiative ionization of C I by hydrogen transitions.

Another theoretical modeling of the non local-thermodynamic-equilibrium (non-LTE) neutral carbon spectral-line formation was made by Fabbian et al. (2006) for stellar abundance analysis. In their study, they focussed on C I lines in the wavelength range of 830–960 nm. These lines are located both in the singlet and the triplet system of C I. The authors found that radiative processes dominate over collisional processes and the non-LTE effects are rather large. In metal-poor stars, also intersystem collisions between the singlet and the triplet systems may also be important. For this reason, Fabbian et al. (2006) also included intersystem collisions with hydrogen, following the Drawin recipe (Drawin 1968, 1969) with a scaling factor. They found that the resulting non-LTE corrections to abundance determinations using these C I lines were not very dependent on the neutral hydrogen collisions.

Avrett & Loeser (2008) solve the non-LTE problem employing an extended C I-C IV model atom with 128 individual energy levels of C I grouped into 19 reference levels. This is done together with non-LTE computations of hydrogen (15 bound levels), O I-O VI (40 levels of O I grouped into 20 reference levels), and 10 other atoms and ions. They produce a semi-empirical model of the quiet solar chromosphere and transition region that reproduces as closely as possible the detailed spectrum observed by SUMER (Curd et al. 2001) with

an additional constraint that the transition region is given by an energy equation containing radiative processes, conduction, and particle diffusion (in contrast with the VAL3C model (Vernazza et al. 1981) where the transition region temperature structure was a fitting function as well).

In this work, we will study the formation of the C I 135.58 nm line in the solar chromosphere employing both a 1D semi-empirical model and a 3D radiation-magnetohydrodynamic (RMHD) model. We will also explore the diagnostic potential of combining the observations in the C I and O I lines. In Section 2 we describe our model atmospheres, radiative transfer computations, and atomic models. In Section 3.1 we discuss the basic formation mechanism and the effects from the hydrogen solution. Following that, we discuss how the dynamics in the atmosphere influences the formation mechanism in Section 3.2 and we present synthetic spectra calculated based on 3D realistic atmospheres. In Section 4 we present their potential diagnostic value, and we conclude in Section 5.

## 2. METHODS

### 2.1. Radiative transfer computations

In this study, we use the RH code (Uitenbroek 2001) to solve the non-LTE radiative transfer problem. RH is a multilevel accelerated lambda iteration code for radiative transfer calculations including PRD. It treats line blending self-consistently. We use the original RH 1D version to study the basic formation mechanism in Section 3.1 with the FALC (Fontenla et al. 1993) atmosphere.

For the 3D atmosphere, we use the 1.5D version of RH (Pereira & Uitenbroek 2015), which treats each column in a 3D atmosphere as an independent plane-parallel atmosphere. The advantage of this version of RH over the original version is that the code is parallelized using the Message Passing Interface (MPI) such that the different columns can be calculated simultaneously. To save computational effort, we do not solve for hydrogen and carbon simultaneously but solve first for hydrogen and store the radiation fields to be used for the carbon solution.

In order to do so accurately, we modified RH so that it stores the ratio between the emissivity and absorption coefficients ( $g_{ij}$  in Eq. (26) of Uitenbroek 2001) for Ly $\alpha$  in the hydrogen calculation. The code then reads these ratios in the computation for carbon and so includes the correct radiation field including PRD effects for the radiative pumping by Ly $\alpha$  in the C I continuum (see Sec. 3.1).

For the hydrogen computation, we also modified RH to maintain the non-equilibrium hydrogen ionization degree as present in the 3D model atmosphere (see Sec. 2.2). We keep the proton density fixed and remove the rate equation for the continuum to keep the rate equations internally consistent. This method is a fairly accurate approximation of the full non-equilibrium non-LTE radiative transfer because the timescales for the ionization balance are long, but the excited levels of hydrogen adapt very fast and can thus be treated assuming statistical equilibrium. For further details, we refer the reader to Golding et al. (2017), who discuss this method in the context of helium.

In Sec. 4 we also make use of non-LTE calculations of the O I 135.56 nm line presented in Lin & Carlsson (2015).

### 2.2. Model atmospheres

In this study, we use two model atmospheres. In Section 3.1, we use the semi-empirical solar chromosphere model

FALC (Fontenla et al. 1993) to study the basic formation mechanism. The FALC model is a semi-empirical atmosphere model that describes the atmosphere in an averaged fashion without dynamics, hence is suitable for studying the line formation qualitatively. However, the nature of the solar chromosphere is far from static. To study the radiation from such a dynamic system, we need a more realistic atmosphere model than FALC. We chose to use a model computed with the RMHD code Bifrost (Gudiksen et al. 2011). In Section 3.2, we use a snapshot from the publicly available 3D simulation en024048\_hion (Carlsson et al. 2016). The snapshot extends 24x24x16.8 Mm in physical space, mapped onto a grid of 504x504x496 cells. It covers the upper convection zone, the chromosphere, the transition region and the lower corona and includes a large-scale magnetic field with two polarities separated by about 8 Mm with an average unsigned magnetic field strength in the photosphere of 50 G. This particular snapshot has also been used in the study of the line formations of H $\alpha$  (Leenaarts et al. 2012), Mg II h and k (Leenaarts et al. 2013a,b; Pereira et al. 2013), C II 133.5 nm multiplet (Rathore & Carlsson 2015; Rathore et al. 2015a), and the O I 135.56 nm line (Lin & Carlsson 2015). We refer the reader to Carlsson et al. (2016) for more details on this simulation. We stress here that the purpose of the current work is to investigate the diagnostic potential of the C I 135.58 nm line and not to test the realism of the atmospheric model. It is well known that the employed Bifrost model fails to reproduce observations in several aspects, *e.g.*, chromospheric lines are too narrow in the model on average and several emission lines are too weak. These discrepancies may be due to a lack of numerical resolution in the models or a lack of physical processes like ambipolar diffusion (*e.g.*, Martínez-Sykora et al. 2017). However, for our purposes, it is enough that the model atmosphere contains the proper parameter range (there are both wide lines and strong emission at locations in the simulation but not enough to reproduce the mean profiles).

### 2.3. Quintessential Model Atom

We start with a model atom containing 168 levels with atomic data taken from the HAOS-Diper package (Judge & Meisner 1994). We do not include hydrogen collisions since atomic data for these are highly uncertain and the study by Fabbian et al. (2006) indicates that they are not important. We simplify this model atom for our purposes. In the simplification procedure, we make sure that at each step we get the same intensity from the FALC model atmosphere in the C I 135.58 nm line but also in two other C I lines in the IRIS wavelength range at 135.43 nm and at 135.71 nm. Since the lines we focus on here are within the singlet system and do not have any direct coupling with the triplet system, we start by excluding all states in the triplet system except the ground states. We do still include the radiative recombination rates into the triplet system with the approach given in Lin & Carlsson (2015). The corresponding effective recombination coefficients are listed in Table 1. We then further simplify our model atom by merging levels, following the procedure described in Bard & Carlsson (2008). The term diagram of the final 26-level model atom is shown in Fig. 1 and the corresponding atomic parameters are listed in Table 2. The word "merged" in the level designation means that the level is such a merged super level. The level designation comes from the level with the lowest energy among the merged levels.

## 3. BASIC FORMATION MECHANISM

**Table 1**  
Effective recombination coefficient from the continuum to  $2s^22p^23P_1$  through the triplet states.

|  | Temperature (K) |         |         |         |        |         |         |         |         |
|--|-----------------|---------|---------|---------|--------|---------|---------|---------|---------|
|  | 4500            | 5160    | 6370    | 7970    | 9983   | 20420   | 41180   | 60170   | 100000  |
| $R_{c1}^*$ ( $10^{-19} \text{ m}^3 \text{ s}^{-1}$ ) | 1.30167         | 1.24998 | 1.16755 | 1.08249 | 1.0130 | 1.25747 | 3.99362 | 7.77096 | 13.0163 |

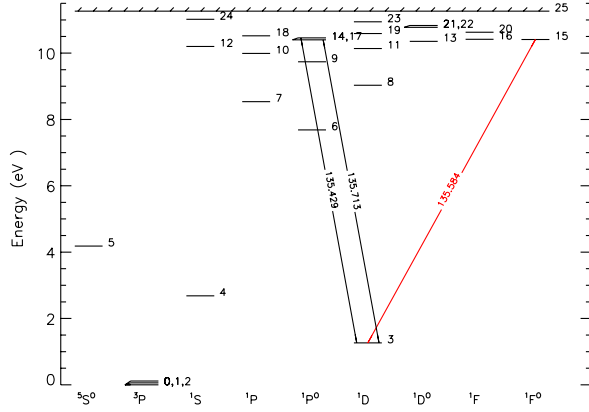


**Figure 1.** Term diagram of the 26-level C I model atom we use in this study. The energies and designations of each numbered level are listed in Table 2. The energies of the levels of the term  $2s^22p^23P$  (levels 0,1,2) are very close to each other and the energy differences within the term are exaggerated in this diagram. The same is true for energy levels 14,17 and 21,22. Only the transitions within the IRIS wavelength range are shown in the diagram with vacuum wavelengths in nm and the transition of special interest here, the C I 135.58 nm line, in red.

**Table 2**  
Atomic parameters for C I.

| Level | Energy [ $cm^{-1}$ ] | Designation                  |
|-------|----------------------|------------------------------|
| 0     | 0.000                | C I $2s^22p^23P_0$           |
| 1     | 16.400               | C I $2s^22p^23P_1$           |
| 2     | 43.400               | C I $2s^22p^23P_2$           |
| 3     | 10192.630            | C I $2s^22p^21D_2$           |
| 4     | 21648.010            | C I $2s^22p^21S_0$           |
| 5     | 33735.200            | C I $2s2p^35S_2^o$           |
| 6     | 61981.820            | C I $2s^22p3s1P_1^o$         |
| 7     | 68856.330            | C I $2s^22p3p1P_1$           |
| 8     | 72838.251            | C I $2s^22p3p1D_2$ -merged   |
| 9     | 78532.462            | C I $2s^22p4s1P_1^o$ -merged |
| 10    | 80562.850            | C I $2s^22p4p1P_1$           |
| 11    | 81769.790            | C I $2s^22p4p1D_2$           |
| 12    | 82251.710            | C I $2s^22p4p1S_0$           |
| 13    | 83497.620            | C I $2s^22p4d1D_2^o$         |
| 14    | 83877.310            | C I $2s^22p5s1P_1^o$         |
| 15    | 83947.430            | C I $2s^22p4d1F_3^o$         |
| 16    | 83997.906            | C I $2s^22p4f1F_3$ -merged   |
| 17    | 84032.150            | C I $2s^22p4d1P_1^o$         |
| 18    | 84851.530            | C I $2s^22p5p1P_1$           |
| 19    | 85399.810            | C I $2s^22p5p1D_2$           |
| 20    | 85717.731            | C I $2s^22p5f1F_3$ -merged   |
| 21    | 86909.475            | C I $2s^22p5d1D_2^o$ -merged |
| 22    | 87083.365            | C I $2s^22p3d1D_2^o$ -merged |
| 23    | 88260.370            | C I $2s^22p7p1D_2$           |
| 24    | 88856.030            | C I $2s^22p7p1S_0$ -merged   |
| 25    | 90859.558            | C II $2s^22p^2P_0$           |

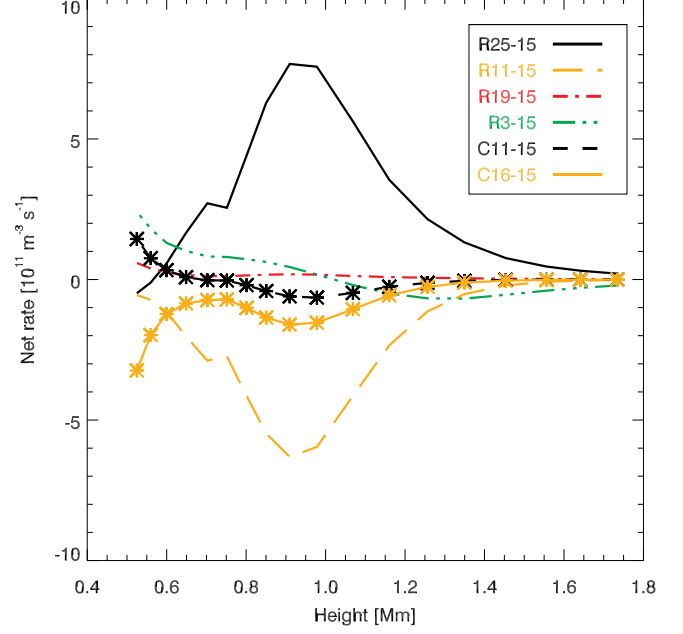


**Figure 2.** Net rates into the upper level of the C I 135.58 nm line,  $2s^22p4d1F_3^o$  (level 15 in the C I model atom shown in Figure 1) in the FALC atmosphere. Positive values denote a net rate into the level, negative values denote a net rate out of the level. Letters R and C in the label stands for radiative net rate and collisional net rate, respectively. The collisional net rates are also overlaid with star symbols. The dominant channel into the  $2s^22p4d1F_3^o$  level is from radiative recombination directly from the continuum (level 25, solid black). The main channel out of level 15 is to the level  $2s^22p4p1D_2$ , (level 11, dashed yellow). The net rate corresponding to the 135.58 nm line, denoted as R15 – 3, (green, dashed-dotted-dotted-dotted), is upward, populating level 15 (positive) below 1 Mm height and is downward (negative) above this height. Collisions to and from the states  $2s^22p4p1D_2$  (level 11) and  $2s^22p4f1F_3$ -merged (level 16) also play a role.

### 3.1. Ionization chain and the line formation

The main ionization process of C I is through photoionization from the  $2s^22p^23P_1$ ,  $2s^22p^23P_2$  and  $2s^22p^21D_2$  states with photoionization from the  $2s^22p^21D_2$  state being dominant.  $2s^22p^21D_2$  is also the lower state of the C I 135.58 nm line and it is mainly populated from the ground term  $2s^22p^23P$  by collisions. The C II ground state is depopulated through radiative recombination to all excited states, followed by radiative cascading.

The upper state of the C I 135.58 nm line,  $2s^22p4d1F_3^o$ , is populated by radiative recombination from the continuum, and depopulated mostly to the state  $2s^22p4p1D_2$ . The C I 135.58 nm line ( $2s^22p4d1F_3^o - 2s^22p^21D_2$ ), is, however, not the dominant channel of depopulating  $2s^22p4d1F_3^o$ .

The net rates for the  $2s^22p4d1F_3^o$  and  $2s^22p^21D_2$  levels are shown in Fig. 2 and Fig. 3, respectively.

The net-rate analysis shows that the ionization degree of neutral carbon is set by photoionization/radiative recombination and is therefore sensitive to the radiation field. Pho-

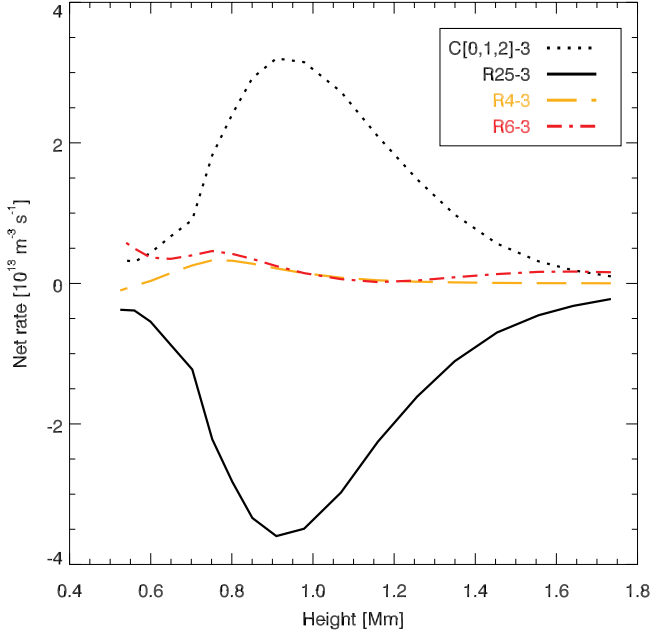


**Figure 3.** Net rates into the lower level of the C I 135.58 nm line,  $2s^22p^2^1D_2$  (level 3 in the C I model atom, see Figure 1). This level is populated (positive net rate) mostly from the ground term,  $2s^22p^2^3P$  by collisions (dotted black). The dominant depopulation channel (negative net rate) is photoionization (solid black) with some return flow through recombination to excited levels followed by cascading ending up through levels 4 and 6 (denoted R4-3, R6-3 here, dashed brown and dotted-dashed red, respectively).

photoionization from the  $2s^22p^2^1D_2$  level requires photons with wavelength below 123.96 nm. This photoionization edge is just long-ward of the hydrogen Ly $\alpha$  line at 121.2 nm and the photoionization rate is therefore sensitive to the Ly $\alpha$  intensity (Lites & Cook 1979). Although the Ly $\alpha$  intensity is highest close to the line core, for the integrated photoionization rate, its wide wings are important. Therefore, the treatment of the frequency redistribution of photons in Ly $\alpha$  is important. Assuming complete frequency redistribution (CRD) leads to an overestimate of the wing intensities, and therefore also of the photoionization rate, compared with the proper treatment with partial frequency redistribution (PRD, see Fig. 4.)

We quantify this by defining the following ratio  $R$  of photoionization rates:

$$R = \frac{\int_{\nu_0}^{\infty} \frac{\sigma_{3c}(\nu)}{h\nu} J_{\nu}(\text{PRD/CRD}) d\nu}{\int_{\nu_0}^{\infty} \frac{\sigma_{3c}(\nu)}{h\nu} J_{\nu}(\text{No Ly}\alpha) d\nu} \quad (1)$$

where  $\sigma_{3c}$  is the photoionization cross-section from the  $2s^22p^2^1D_2$  level to the continuum,  $J_{\nu}(\text{CRD/PRD})$  is the radiation field with hydrogen lines in CRD/PRD respectively, and  $J_{\nu}(\text{No Ly}\alpha)$  is the radiation field without Ly $\alpha$  emission. This ratio thus quantifies the effect of the Ly $\alpha$  line on the photoionization of C I. We show  $R$  as a function of height in the FALC model in Fig. 5. It is unity in the deep atmosphere but becomes larger above 0.5 Mm height. With the assumption of CRD in the Ly $\alpha$  line, the ratio becomes much larger than when assuming PRD owing to the extended Ly $\alpha$  wings in CRD.

Finally, we compare the O I 135.56 nm and the C I 135.58 nm lines that are calculated based on treating Ly $\alpha$  in PRD, CRD, and excluding the line altogether in Fig. 6. There are substantial differences in the resulting C I 135.58 nm line. The stronger the C I photoionization the stronger the line, which

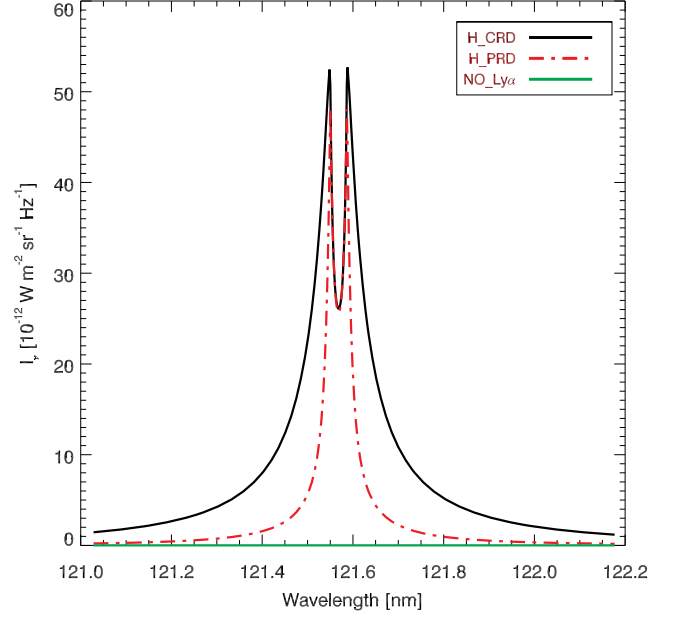


**Figure 4.** Vertically emergent intensity from the FALC model with different treatments of the Ly $\alpha$  line. Ly $\alpha$  in CRD (black), in PRD (red dash-dotted), and without the Ly $\alpha$  (green).

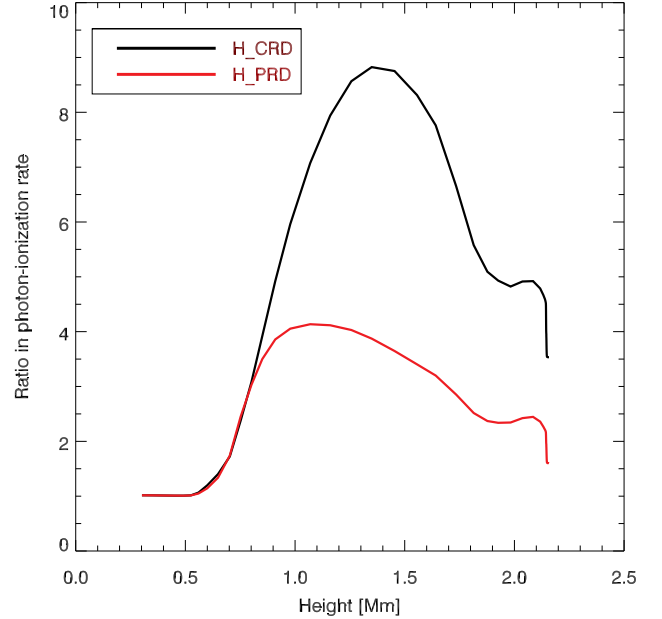


**Figure 5.** Ratio of the C I photoionization rate in the FALC model atmosphere with the Ly $\alpha$  line profiles treated with CRD (black) and PRD (red) with respect to the case without Ly $\alpha$  line emission. The definition of the ratio is given in Eq. (1).

is consistent with the result that the upper level of the line is populated mainly through photorecombinations from C II.

To summarize the basic formation mechanism of the C I 135.58 nm line, we show the dominant channels of the C I formation in Fig. 7.

### 3.2. Line formation in a dynamic atmosphere

So far, we have studied the basic line-formation mechanisms using the 1D, static, semi-empirical model atmosphere



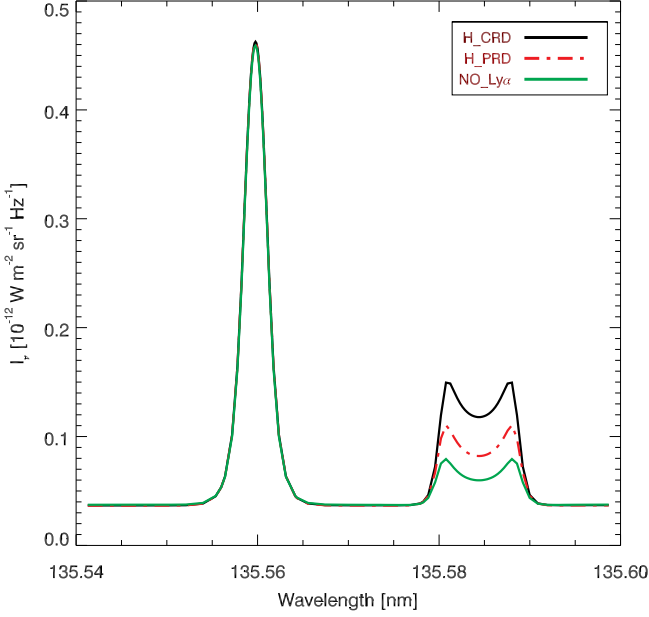


**Figure 6.** Resulting O I and C I line intensity with different treatments of the Ly $\alpha$  line. Black: Ly $\alpha$  in CRD; red dotted-dashed: Ly $\alpha$  in PRD; green: no Ly $\alpha$  line.

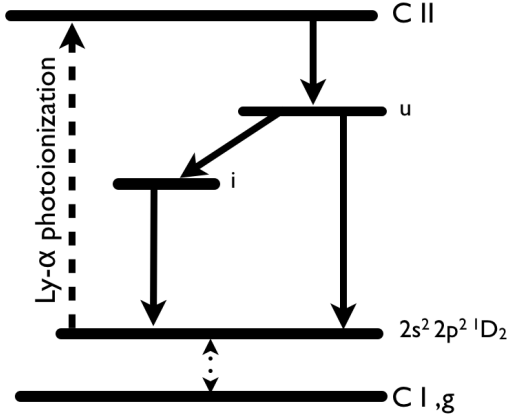


**Figure 7.** Schematic C I term diagram that summarizes the basic formation mechanism of the C I 135.58 nm line. The solid lines represent radiative cascading, the dashed line photoionization, and the dotted line stands for collisions. The ionization degree of C I is set by two steps: first a collisional coupling from the ground term to  $2s^2 2p^2 \ ^1D_2$  and then photoionization by the radiation field blueward of 123.96 nm, including an important contribution from hydrogen Ly $\alpha$  emission. The upper level of the 135.58 nm line, marked with “u”, is populated by radiative recombination. The downward rate from “u” channel through intermediate states, denoted as “i”, or directly back to  $2s^2 2p^2 \ ^1D_2$ .

FALC. We now turn to how the C I 135.58 nm line is formed in a more realistic atmosphere with velocity fields. For this purpose, we use the Bifrost simulation en024048\_hion (Carlsson et al. 2016). To illustrate the line formation, we use the four-panel diagrams introduced by Carlsson & Stein (1997).

The vertically emergent intensity in a 1D plane-parallel semi-infinite atmosphere can be written as

$$I_V = \int_0^\infty S_V(z) e^{-\tau_V(z)} \chi_V(z) dz.$$

where  $S_V$ ,  $\chi_V$ , and  $\tau_V$  are the source function, opacity, and

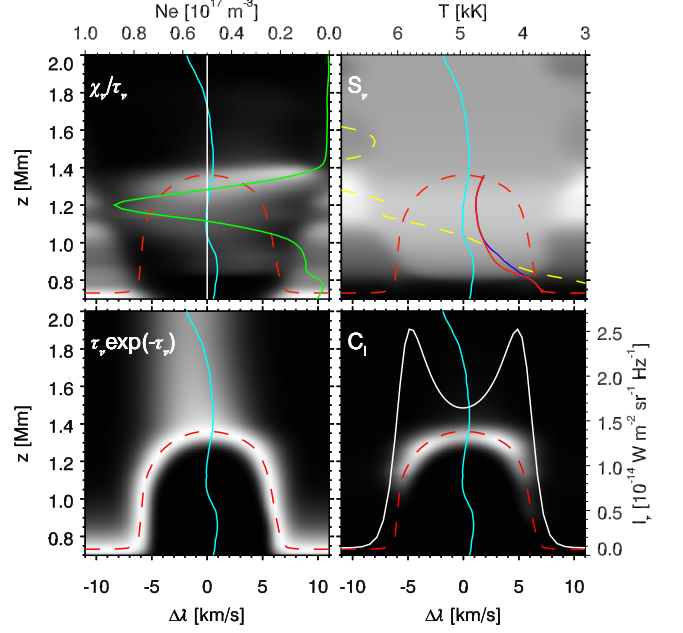


**Figure 8.** Intensity formation of the C I 135.58 nm line in a column of the 3D atmosphere characterized by moderate velocities and almost zero velocity gradients. The label in the top-left corner of each panel shows the quantity shown as a grayscale image as a function of doppler shift from the rest wavelength (positive is redshift) and height  $z$ . The  $\tau_V = 1$  height is outlined as a red-dashed line and the vertical velocity as a turquoise solid line in all four panels. The white straight line in the upper left panel shows the rest wavelength, and the green solid line gives the electron density with a scale at the top. In the panel of  $S_V$  (top right), the dashed yellow curve denotes the temperature as function of height  $z$ , while the solid curves denote the value of the source function at a given height at the wavelength that has  $\tau_V = 1$  at that height on the red-side (red line), and blue-side (blue line) of the  $\tau_V = 1$  maximum. They are given in radiation temperature units with the scale given at the top. In the lower right panel, we show the full contribution function (the product of the terms shown as grayscale images in the other three panels) together with the emergent intensity profile with a scale to the right. The line profile is symmetric with two emission peaks and a central depression. These emission peaks are formed where there is a local maximum in the source function and the central depression is caused by the decreasing source function at this height.

optical depth, respectively.

In this equation, the integrand describes the local creation of photons ( $S_V(z)\chi_V(z)dz$ ) and the fraction of those that escape ( $e^{-\tau_V(z)}$ ), and the integrand is thus a natural definition of the contribution function to intensity on a height scale.

$$C_{I_V}(z) = S_V(z) e^{-\tau_V(z)} \chi_V(z).$$

We can rewrite this contribution function as

$$C_{I_V}(z) = S_V(z) \tau_V(z) e^{-\tau_V(z)} \frac{\chi_V(z)}{\tau_V(z)}$$

where the term  $\tau_V(z) e^{-\tau_V(z)}$  peaking at  $\tau_V = 1$  represents the Eddington-Barbier part of the contribution function,  $S_V(z)$  gives the source function contribution and  $\chi_V(z)/\tau_V(z)$  picks out effects of velocity gradients in the atmosphere (see Carlsson & Stein 1997).

Fig. 8 shows the intensity formation of the C I 135.58 nm line in an atmospheric column with moderate velocities and almost no velocity gradients. The intensity is formed close to  $\tau_V = 1$  as indicated by the maximum of the contribution function following the  $\tau_V = 1$  curve. The continuum is formed at a height of 0.73 Mm, where the temperature is 3 kK but with a decoupled source function at a radiation temperature of

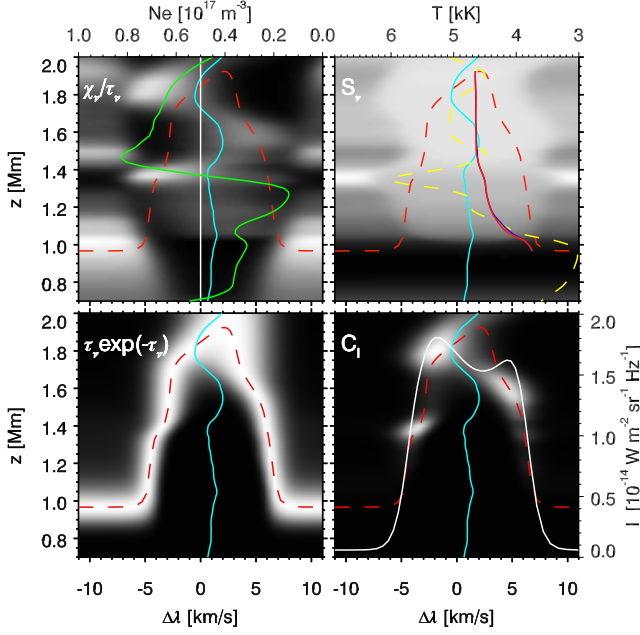


**Figure 9.** As Fig. 8 but for a column of the 3D atmosphere characterized by moderate velocities and moderate velocity gradients. The intensity profile has two peaks, as is the case in Fig. 8, but the cause is quite different: The source function is rather constant with height and the two maxima of the contribution function are caused by velocity gradients (the term that is shown in the upper left panel) rather than by a local maximum of the source function.

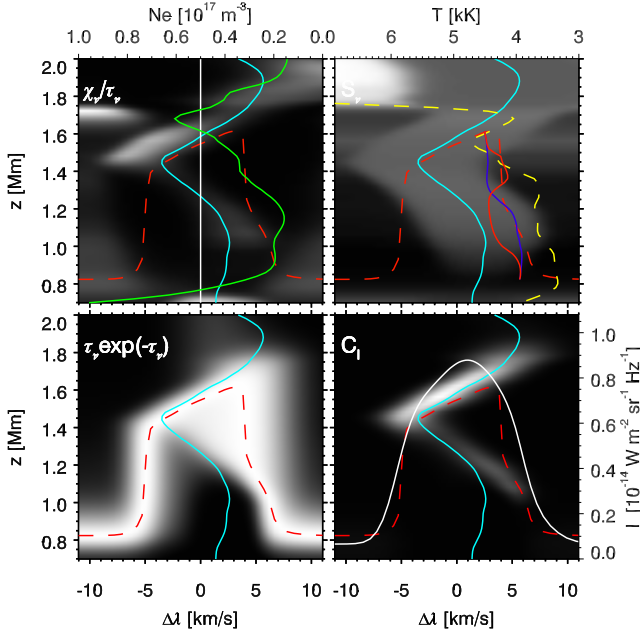


**Figure 10.** Same as Fig. 8 but for a column of the 3D atmosphere characterized by strong velocities and strong velocity gradients. The formation of the line is driven by the velocity gradient and we do not observe a decreasing source function with height. This results in a singly peaked line profile.

3.7 kK. The line core has optical depth unity at  $z = 1.35$  Mm. The upper right panel shows that the source function increases up to  $z = 1.2$  Mm and decreases higher up. The local maximum of the source function is the reason for the two emission peaks and the central reversal.

Fig. 9 shows the intensity formation at another column in the atmosphere where the velocities are larger and there are significant velocity gradients in the line forming region. The

intensity profile (shown in the lower right panel) still has two peaks and a central reversal but the reason is different from the case shown in Fig. 8. The source function (upper right panel) is rather constant with height above  $z = 1.5$  Mm, which would give a single peak intensity profile with a flat top. The reason we still get two emission peaks is that the velocity gradients around the velocity maxima at  $z = 1.8$  Mm and  $z = 1.6$  Mm give large  $\chi_v/\tau_v$  terms (upper left panel).

A third example is given in Fig. 10. At this column of the atmosphere, there is a strong velocity gradient above  $z = 1.5$  Mm influencing both the  $\tau_v = 1$  shape with its maximum height at a redshift of  $4 \text{ km s}^{-1}$  and the intensity profile. The source function (the relevant one for the profile blueward of  $+4 \text{ km s}^{-1}$  is given by the blue line in the upper right panel) is slowly decreasing above  $z = 1.4$  Mm but the  $\chi_v/\tau_v$  term decreases with increasing redshift, so we get a maximum intensity at a redshift of  $1 \text{ km s}^{-1}$ .

From the selected cases shown above, we learn that the line profile is influenced both by the run of the source function with height and by velocity gradients in the atmosphere.

#### 4. DIAGNOSTIC POTENTIAL

Spectral line-profiles encode information from the conditions in the atmosphere where the photons escape. To decode this information, we need to find the line-forming region and then correlate observable quantities with atmospheric parameters in this region. We start this section with a discussion of the line-forming region.

##### 4.1. The line core

As we have seen in the previous section, the C I 135.58 nm line has a typical optically thick line-formation with the contribution function to intensity centered around monochromatic optical depth unity. The maximum height we can get information from is at the wavelength where this optical depth unity is the highest. This wavelength is not immediately available observationally. In the absence of velocity fields, we have the maximum opacity at the rest wavelength of the transition, which is also the wavelength of maximum optical-depth-unity height. If the source function is monotonically increasing with height, we get an emission line with the maximum intensity at this wavelength. If there is a local maximum in the source function below the optical-depth-unity height at line center, we get an emission line with a self-reversal. Dependent on the source function variation with height, we may also get more than two peaks in the intensity profile. In the absence of velocity fields, the line center is at the position of the central emission maximum for profiles with an odd number of peaks and at the position of the central emission minimum for profiles with an even number of peaks. We use this wavelength as our observationally defined line-core wavelength in spite of the fact that, as we have seen in Section 3.2, velocity gradients may strongly affect the contribution function to intensity and the correlation between this observationally defined line core wavelength and the wavelength of maximum  $\tau_v = 1$  height.

In the following, we inspect various quantities at this wavelength.

##### 4.2. The Contribution function

In Fig. 11 we show the contribution function to intensity at the line-core wavelength (as defined in Sec. 4.1) along a selected cut at  $x = 12$  Mm in Fig. 12. The red line in Fig. 11

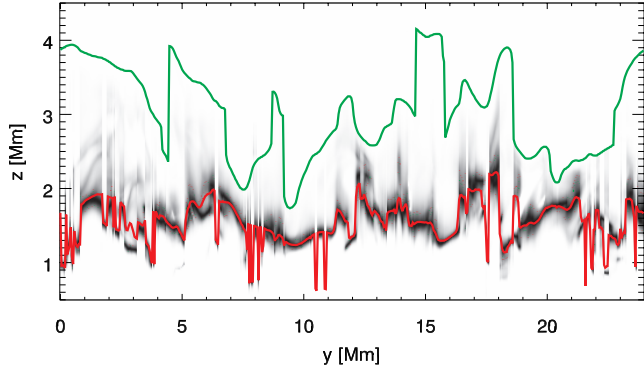


**Figure 11.** Contribution function to the intensity at the wavelength of the C I 135.58 nm line core along the  $x = 12$  Mm cut through the atmospheric model (Fig. 12) shown as a grayscale image. The line core wavelength is defined as the wavelength of the central emission peak for profiles with an odd number of emission peaks and as the wavelength of the central absorption for profiles with an even number of emission peaks. Also shown are the  $\tau_v = 1$  height for this same wavelength (red) and the temperature contour at 30 kK (green). The contribution function is normalized at each  $y$ -value. Note also that the aspect ratio is with an expanded height scale. The maximum of the contribution function closely follows the  $\tau_v = 1$  height, consistent with a typical optically thick formation.

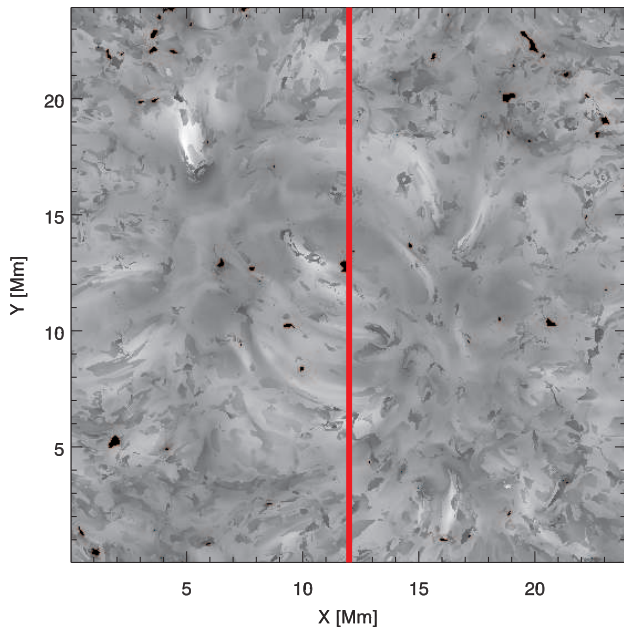


**Figure 12.** Formation height of the C I line core. The cut indicated with a red line at  $x = 12$  Mm gives the 2D cut used in Fig. 11.

represents the  $\tau_v = 1$  height. It is clear that the maximum of the contribution function to intensity is tightly correlated with this height, consistent with an optically thick formation of the line.

#### 4.3. Formation height

As the C I line has an optically thick formation, the  $\tau_v = 1$  height could be a natural choice for its formation height. However, to be consistent with the treatment with the O I 135.56 nm line (Lin & Carlsson 2015), we follow the same definition for the C I 135.58 nm line and use the contribution-function-weighted averages to define the formation height and

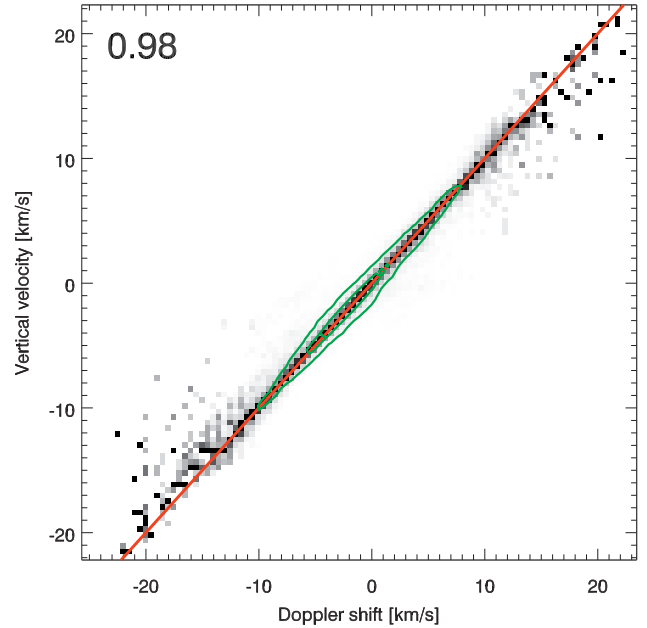


**Figure 13.** Probability density function (PDF) of the contribution-function-weighted vertical velocity as function of the Doppler shift of the line-core. The Pearson correlation coefficient is shown in the upper left corner. The green inner contour encloses 50% of all pixels and the outer contour 90%. The diagonal red straight line denotes  $y = x$ . The correlation is quite tight, which makes the C I 135.58 nm line a good velocity diagnostic.

other quantities:

$$X_{\text{fh}} = \frac{\int_0^{\infty} C_I(z)X(z)dz}{\int_0^{\infty} C_I(z)dz}, \quad (2)$$

where  $X$  is the quantity under consideration and  $X_{\text{fh}}$  is its contribution-function-weighted average.

The result for the contribution-function-weighted C I 135.58 nm line-formation height is shown in Fig. 12. The loop-like features show the influence of the magnetic structures on the line opacity. At some points, the formation height is very much lower than at neighboring points (seen as darker small patches, also visible along the selected cut shown in Fig. 11). These deviating formation heights are associated with the algorithm for selecting the line core wavelength not finding the actual wavelength of the maximum  $\tau_v = 1$  height.

In the further analysis in this section, we use plasma properties calculated using Eq. 2.

#### 4.4. Velocity

With the line-core frequency defined in Sec. 4.1, we can obtain the Doppler shift with respect to the rest frequency and compare with the contribution-function-weighted vertical velocity. In Fig. 13 we find the correlation to be quite tight, making C I 135.58 nm line a good velocity diagnostic.

#### 4.5. Electron density

It is interesting to investigate the diagnostic power of the O I 135.56 nm line and the C I 135.58 nm line combined, because they are observed together with IRIS.

As discussed in Lin & Carlsson (2015), the O I 135.56 nm line intensity is proportional to the square of the electron density: the line is formed by recombination from O II followed by radiative cascading to the upper level of the transition.

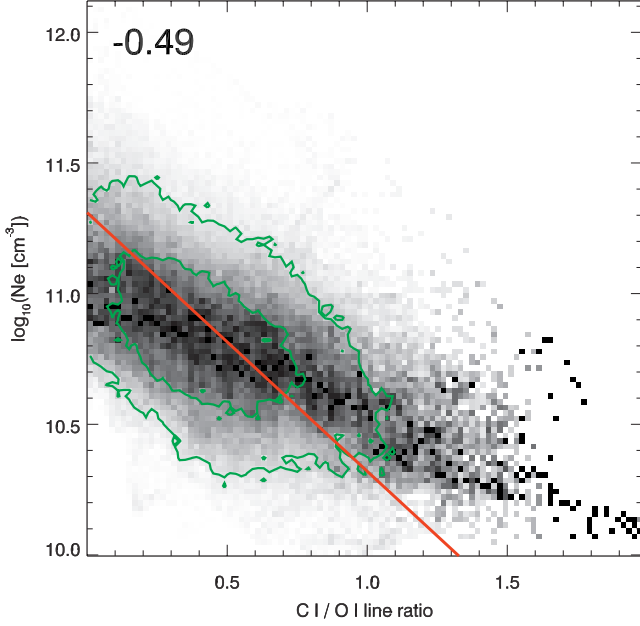


**Figure 14.** PDF of the electron density as a function of the C I/O I total line intensity ratio. The Pearson correlation coefficient is shown in the upper left corner. The green inner contour encloses 50% of all pixels and the outer contour 90%. The red straight line representing  $y = -x + 11.31$  indicates  $I(\text{C I})/I(\text{O I}) \sim 1/N_e$ .

The recombination rate scales linearly with the electron density. The O II density is proportional to the proton density (and hence the electron density), which combined yields the quadratic dependence.

In Section 3.1 we show that the C I 135.58 nm line formation is driven by ionization by  $\text{Ly}\alpha$  photons followed by radiative recombinations. Such a process scales linearly with the electron density (through the recombination) but of course will also be dependent on the  $\text{Ly}\alpha$  radiation field. As a result, we anticipate that the C I/O I line ratio scales as  $\sim J(\text{Ly}\alpha)/N_e$ , where  $J(\text{Ly}\alpha)$  is the radiation field in the  $\text{Ly}\alpha$  transition. In Fig. 14 we show the correlation between the electron density at the average formation height and the C I/O I line ratio. It shows a roughly linear correlation, but with a considerable spread.

#### 4.6. Formation height difference

From the histogram of the formation heights of the O I 135.56 nm line and the C I 135.58 nm line (Fig. 15), it is clear that these two lines map slightly different layers in the atmosphere. In general, the C I 135.58 nm line forms higher than the O I 135.56 nm line. The distribution of the C I 135.58 nm line peaks around 1.5 Mm, while the O I 135.56 nm line distribution peaks around 1.2 Mm.

The two lines have different sensitivity to the electron density (see Fig. 14). This also means that there is a correlation between the C I/O I line-core intensity ratio and the formation height difference — a low intensity ratio corresponds to a high intensity oxygen line formed low down and thus with a large formation height difference. This correlation is shown in Fig. 16. The correlation is clear but the spread is rather large.

#### 4.7. The velocity difference and the velocity gradient

Because the O I 135.56 nm line and the C I 135.58 nm line probe slightly different layers in the atmosphere and their

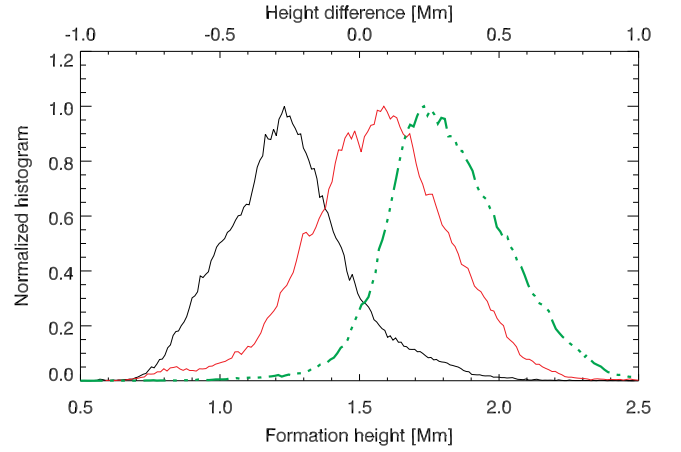


**Figure 15.** Histograms of the formation height of the O I 135.56 nm line (black), the C I 135.58 nm line (red) with the axis below. The histogram of the formation height difference (C I - O I) is given as a green dash-dotted line with the axis at the top. The C I line forms mostly higher than the O I line.

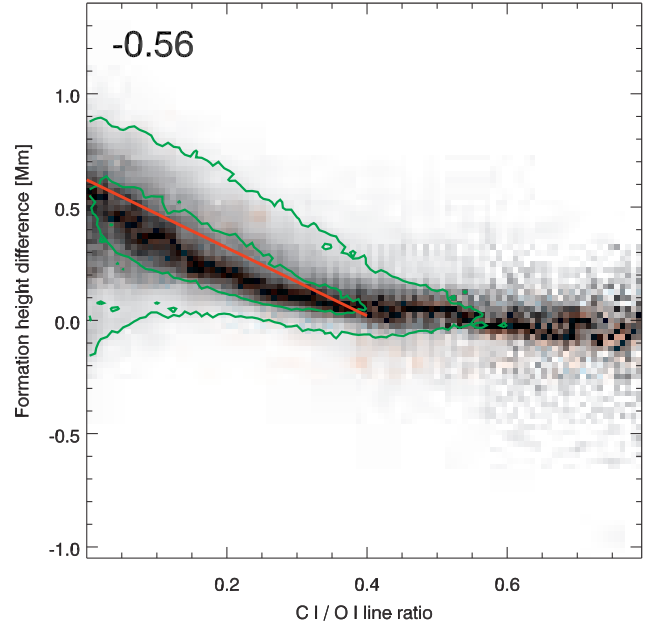


**Figure 16.** PDF of the formation height difference [C I - O I] as a function of the C I/O I line-core intensity ratio. The Pearson correlation coefficient is shown in the upper left corner. The green inner contour encloses 50% of all pixels and the outer contour 90%. The red straight line denotes  $y = -1.5x + 0.62$ .

Doppler shifts are good velocity indicators, it is possible to take the difference between their individual Doppler shifts and measure the velocity difference between these two layers. In Fig. 17 we show the correlation between the difference between the contribution-function-weighted velocities of the lines and the difference of their individual Doppler shifts. The correlation is strong. Together with the correlation between the line ratio and the formation height difference (Fig. 16), it is possible to derive a rough estimate of the velocity gradient in the middle chromosphere.

## 5. DISCUSSION AND CONCLUSIONS

We presented an analysis of the formation of the C I 135.58 nm line in the FALC 1D semi-empirical atmosphere model and a 3D RMHD model computed with the



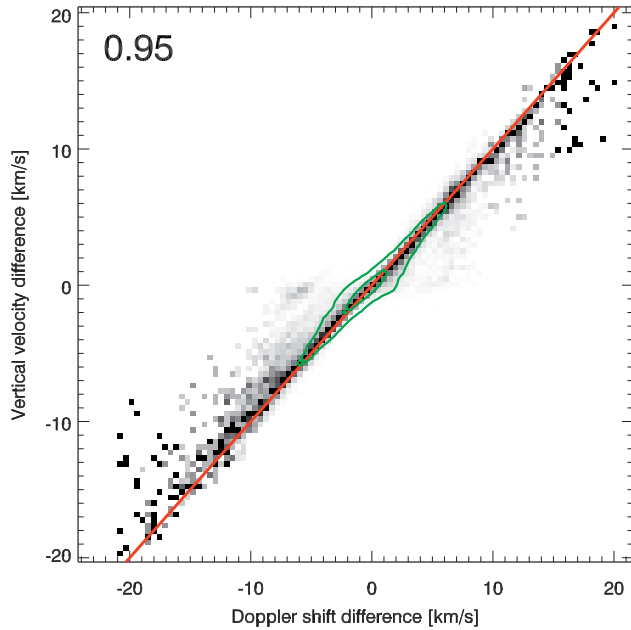


**Figure 17.** PDF of the difference in correlation-function-weighted vertical velocity between the C I and the O I lines as a function of the Doppler shift difference. The Pearson correlation coefficient is shown in the upper left corner. The green inner contour encloses 50% of all pixels and the outer contour 90%. The diagonal red straight line denotes  $y = x$ .

Bifrost code. We show that the line has a typical optically thick line formation.

The C I/C II ionization balance is mainly driven by photoionization from  $2s^2 2p^2 \ ^1D_2$ , with the radiation field in Ly $\alpha$  playing a central role. Proper modeling of the C I 135.58 nm line should therefore incorporate non-LTE modeling of hydrogen including PRD in the Ly $\alpha$  line. In a static atmosphere, the line core usually appears with a central reversal, due to a local maximum of the source function below the maximum  $\tau_v = 1$  height. However, if velocity gradients are present in the atmosphere then the line profiles can have more different, usually asymmetric, shapes. Interestingly, we find some instances where a strong velocity gradient close to the line-core formation height can cause a single-peaked profile in spite of a source function decreasing with height at the maximum  $\tau_v 1$  height (which would lead to a central reversal in the absence of the velocity gradient). We also find cases of the opposite: velocity gradients leading to a central reversal even though the source function monotonically increases with height.

The Doppler shift of the line core is a good velocity diagnostic.

The C I 135.58 nm line can be combined with the nearby O I 135.56 nm line for increased diagnostic power. The C I 135.58 nm line typically forms slightly higher than the O I 135.56 nm line, and both are good velocity diagnostics. The difference in their Doppler-shifts is therefore a good indicator of the velocity difference between their formation layers. By combining this with the correlation of the C I/O I line ratio and the formation height difference one can derive an estimate of the actual velocity gradient. Because the line ratio - height difference correlation is weak and has considerable spread, this estimate is, however, rather coarse.

Furthermore, we find that the C I/O I total line intensity ratio is inversely proportional to the electron density:  $I(\text{C I})/I(\text{O I}) \sim 1/N_e$ , but again with a large spread in the cor-

relation.

We stress that these relations have been derived from a Bifrost model snapshot that is typical of the quiet Sun. A flare (where the C I 135.58 nm line is often stronger than the O I 135.56 nm line) has very different atmospheric properties and the relations derived here cannot be used under such conditions.

We also note that all correlations are derived from radiative transfer calculations using the 1.5D approximation. The Ly $\alpha$  line is, however, strongly influenced by 3D effects (Štěpán et al. 2015; Sukhorukov & Leenaarts 2017), and this might have an influence on the results presented here.

## REFERENCES

- Avrett, E. H., & Loeser, R. 2008, *ApJS*, 175, 229
- Bard, S., & Carlsson, M. 2008, *ApJ*, 682, 1376
- Carlsson, M., Hansteen, V. H., Gudiksen, B. V., Leenaarts, J., & De Pontieu, B. 2016, *A&A*, 585, A4
- Carlsson, M., & Stein, R. F. 1997, *ApJ*, 481, 500
- Cheng, C. C., Feldman, U., & Doschek, G. A. 1980, *A&A*, 86, 377
- Curdt, W., Brekke, P., Feldman, U., et al. 2001, *A&A*, 375, 591
- Drawin, H.-W. 1968, *Zeitschrift fur Physik*, 211, 404
- Drawin, H. W. 1969, *Zeitschrift fur Physik*, 225, 483
- Fabbian, D., Asplund, M., Carlsson, M., & Kiselman, D. 2006, *A&A*, 458, 899
- Fontenla, J. M., Avrett, E. H., & Loeser, R. 1993, *ApJ*, 406, 319
- Golding, T. P., Leenaarts, J., & Carlsson, M. 2017, *A&A*, 597, A102
- Gudiksen, B. V., Carlsson, M., Hansteen, V. H., et al. 2011, *A&A*, 531, A154
- Judge, P. G., & Meisner, R. W. 1994, in *ESA Special Publication*, Vol. 373, *Solar Dynamic Phenomena and Solar Wind Consequences, the Third SOHO Workshop*, ed. J. J. Hunt, 67
- Leenaarts, J., Carlsson, M., & Rouppe van der Voort, L. 2012, *ApJ*, 749, 136
- Leenaarts, J., Pereira, T. M. D., Carlsson, M., Uitenbroek, H., & De Pontieu, B. 2013a, *ApJ*, 772, 89
- . 2013b, *ApJ*, 772, 90
- Lin, H.-H., & Carlsson, M. 2015, *ApJ*, 813, 34
- Lites, B. W., & Cook, J. W. 1979, *ApJ*, 228, 598
- Martínez-Sykora, J., De Pontieu, B., Hansteen, V. H., et al. 2017, *Science*, 356, 1269
- Mauas, P. J., Avrett, E. H., & Loeser, R. 1989, *ApJ*, 345, 1104
- Pereira, T. M. D., Leenaarts, J., De Pontieu, B., Carlsson, M., & Uitenbroek, H. 2013, *ApJ*, 778, 143
- Pereira, T. M. D., & Uitenbroek, H. 2015, *A&A*, 574, A3
- Rathore, B., & Carlsson, M. 2015, *ApJ*, 811, 80
- Rathore, B., Carlsson, M., Leenaarts, J., & De Pontieu, B. 2015a, *ApJ*, 811, 81
- Rathore, B., Pereira, T., Carlsson, M., & De Pontieu, B. 2015b, *ApJ*, 814, 70
- Sukhorukov, A. V., & Leenaarts, J. 2017, *A&A*, 597, A46
- Uitenbroek, H. 2001, *ApJ*, 557, 389
- Štěpán, J., Trujillo Bueno, J., Leenaarts, J., & Carlsson, M. 2015, *ApJ*, 803, 65
- Vernazza, J. E., Avrett, E. H., & Loeser, R. 1981, *ApJS*, 45, 635